Computers in Biology and Medicine 145 (2022) 105423

Contents lists available at ScienceDirect

Computers in Biology and Medicine

journal homepage: www.elsevier.com/locate/compbiomed

Automated detection and classification of tumor histotypes on dynamic PET imaging data through machine-learning driven voxel classification

G. Bianchetti [a,c], S. Taralli [b], M. Vaccaro [c], L. Indovina [c], M.V. Mattoli [d], A. Capotosti [c], V. Scolozzi [b], M.L. Calcagni [b,e], A. Giordano [b,e], M. De Spirito [a,c,1], G. Maulucci [a,c,*,1]

[a] Neuroscience Department, Biophysics Section, Università Cattolica del Sacro Cuore, 00168, Rome, Italy
[b] Dipartimento di Diagnostica per Immagini, Radioterapia Oncologica ed Ematologia, Unità di Medicina Nucleare, Fondazione Policlinico Universitario A. Gemelli IRCCS, Rome, Italy
[c] Fondazione Policlinico Universitario "A. Gemelli", IRCCS, 00168, Rome, Italy
[d] Department of Neurosciences, Imaging and Clinical Sciences, "G. D'Annunzio" Chieti-Pescara University, Chieti, Italy
[e] Dipartimento Universitario di Scienze Radiologiche ed Ematologiche, Università Cattolica del Sacro Cuore, Rome, Italy

ARTICLE INFO

Keywords:
Dynamic PET imaging
Machine learning
Automated classification
Lung histotypes
Metastasis

ABSTRACT

2-deoxy-2-fluorine-(^{18}F)fluoro-D-glucose Positron Emission Tomography/Computed Tomography (^{18}F-FDG-PET/CT) is widely used in oncology mainly for diagnosis and staging of various cancer types, including lung cancer, which is the most common cancer worldwide. Since histopathologic subtypes of lung cancer show different degree of ^{18}F-FDG uptake, to date there are some diagnostic limits and uncertainties, hindering an ^{18}F-FDG-PET-driven classification of histologic subtypes of lung cancers. On the other hand, since activated macrophages, neutrophils, fibroblasts and granulation tissues also show an increased ^{18}F-FDG activity, infectious and/or inflammatory processes and post-surgical and post-radiation changes may cause false-positive results, especially for lymph-nodes assessment. Here we propose a model-free, machine-learning based algorithm for the automated classification of adenocarcinoma, the most common type of lung cancer, and other types of tumors. Input for the algorithm are dynamic acquisitions of PET data (dPET), providing for a spatially and temporally resolved characterization of the uptake kinetic. The algorithm consists in a trained Random Forest classifier which, relying contextually on several spatial and temporal features of ^{18}F-FDG uptake, generates as an outcome probability maps allowing to distinguish adenocarcinoma from other lung histotype and to identify metastatic lymph-nodes, ultimately increasing the specificity of the technique. Its performance, evaluated on a dPET dataset of 19 patients affected by primary lung cancer, provides a probability 0.943 ± 0.090 for the detection of adenocarcinoma. The use of this algorithm will guarantee an automatic and more accurate localization and discrimination of tumors, also providing a powerful tool for detecting at which extent tumor has spread beyond a primary tumor into lymphatic system.

1. Introduction

Positron Emission Tomography (PET) constitutes a non-destructive and non-invasive imaging technique to assess the functionality and metabolism of tissues in physiological or pathological conditions [1]. While computed tomography (CT) and magnetic resonance (MR) imaging are based on anatomic changes for diagnosis, staging and follow-up of cancers, PET system relies on the detection of pairs of gamma rays which are released when radionuclides, such as F-18, carbon-11 and oxygen-15, emit positrons that undergo annihilation with electrons [2]. It is well-known that cancer cells reprogram their metabolism and energy production networks, in order to sustain rapid growth and survival rate even in a hypoxic and poor of nutrients environment [3]. The alteration of the glucose metabolism of these cells constitutes the basis ^{18}F-FDG-PET imaging technique, which is regarded as a standard of care in the management of several types of cancer [4,5]. ^{18}F-FDG, a glucose analog with the positron-emitting radionuclide fluorine-18 substituted for the normal hydroxyl group at the C-2 position in the glucose molecule, is the most widely and successfully used radiotracer for the detection of cancerous tissues. ^{18}F-FDG-PET/CT is

* Corresponding author. Neuroscience Department, Biophysics Section, Università Cattolica del Sacro Cuore, 00168, Rome, Italy.
E-mail address: giuseppe.maulucci@unicatt.it (G. Maulucci).
[1] Senior Authors.

https://doi.org/10.1016/j.compbiomed.2022.105423
Received 14 January 2022; Received in revised form 11 March 2022; Accepted 17 March 2022
Available online 29 March 2022

widely used in oncology mainly for diagnosis and staging of various cancer types, including lung cancer, which is the most common cancer worldwide [6]. Since histopathologic subtypes of lung cancer show different degree of ^{18}F-FDG uptake, to date there are some diagnostic limits and uncertainties, hindering an ^{18}F-FDG-PET-driven classification of histologic subtypes of lung cancers [7,8]. Moreover, difference in tracer avidity between tumors and non-neoplastic tissues affects the diagnostic accuracy of ^{18}F-FDG uptake. Indeed, among several factors, a suboptimal preparation of patients with glucose intolerance or diabetes and high physiological FDG activity in organs such as brain and liver, can render the signal-to-noise ratio unfavorable for lesion detection, causing false-negative results. On the other hand, infectious and/or inflammatory processes, as well as post-surgical and post-radiation changes may cause false-positive results, especially in lymph-nodes where activated macrophages, neutrophils, fibroblasts and granulation tissues show an increased ^{18}F-FDG activity [9].

Aiming to overcome such diagnostic limits of PET imaging, in recent years, machine learning (ML)-based applications in metabolic imaging have received growing attention [10–13]. Thanks to application of ML algorithms for image processing and classification tasks, nuclear imaging has benefited by improvements in cancer staging and restaging, identification of the radiation treatment gross tumor volume, monitoring of disease, prediction of outcomes and personalization of treatment regimens [14]. The most successful applications are found through multi-modal imaging approaches, especially in combination with CT [14]. However, images processed by PET-CT scanners, though allowing the acquisition of functional and anatomical information in the same session, suffer from artifacts in the fusion image due to physiologic motions (e.g., cardiac and respiratory motions), especially for the assessment of primary lung lesions. The occurring spatial misregistration hampers the adoption of analysis methods relying on this comparison [15,16]. For thoracic and abdominal lesions, a ML-based automated detection tool able to localize and distinguish different types of tumors from other non-neoplastic tissues characterized by high ^{18}F-FDG uptake is therefore still missing. To pursue this objective, active research has focused on dynamic acquisitions of PET (dPET) data, allowing for a deeper metabolic characterization of the detected area through the acquisition of the temporally resolved ^{18}F-FDG uptake with voxel resolution [17,18]. Metabolic rates are usually separated from transport effects and determined from the dynamically acquired PET data by applying mathematical models of tracer kinetics from blood into tissues [19–22]. However, several factors, including the method of defining regions of interest (ROIs) and the reconstruction parameters used [23] as well as noise, image resolution [24] and instrumentation factors [25,26], can influence the quantification of tracer uptake in a tumor. In addition, since the blood activity concentration over time is needed as an input function for mathematical modeling, this approach requires an invasive continuous monitoring of blood tracer concentration [27–29]. In this context, the application of ML techniques to dPET data can be a key for the development of a data-driven classification of the tumor ^{18}F-FDG uptake with improved performance. However, existing applications of ML on dPET still require kinetic modeling, and were not anyway tested to distinguish and classify histotypes of tumors which are characterized by different kinetics of ^{18}F-FDG uptake [30].

Here we propose a model-free, ML-based method for the automated detection and classification of adenocarcinomas (AD), the most common type of lung cancer, accounting for approximately one-half of lung cancer cases [31,32], and other tumors' histotypes (i.e. large cell neuroendocrine carcinoma, LCNEC, and squamous cells carcinoma, SqCC), evaluating its performance on a dPET dataset of 19 patients affected by primary lung cancer. This technique consists in a trained Random Forest classifier which can classify contextually ^{18}F-FDG uptake spatial and temporal features, such as intensity, edges, and texture of the detected region, providing for the generation of probability maps allowing to discern and localize objects with different kinetics of tracer uptake, such as AD and other cancer histotypes. Moreover, the classification algorithm can associate to each voxel a probability that the tumor has spread in regions outside lung parenchyma, such as lymph-nodes. This is very important, and its further development may assist the physician in the correct identification of distant neoplastic regions. This approach, being independent of the theoretical and experimental biases due to the definition and application of a mathematical model, can lead to an accurate classification of lung lesions, constituting also a potentially powerful tool for the early and non-invasive detection of metastasis and/or other pathological metabolic abnormalities.

2. Materials and methods

2.1. Selection of patients

We prospectively evaluated 19 patients (6 females, 13 males; mean age = 70.1 ± 7.7 years) with histologically proved primary lung cancer (19 non-small cell lung cancer) referred from the Thoracic Surgery Unit of San Camillo Forlanini Hospital (Rome, Italy) to the PET-CT center of the Fondazione Policlinico Universitario "A. Gemelli" IRCCS (Rome, Italy). A cohort of these patients was previously investigated in a study by our group, with different aims [33]. This study was approved by the local Ethics Committee. All the clinical investigations were conducted according to the principles expressed in the Declaration of Helsinki and all patients provided informed consent.

The epidemiological characteristics of the patients, the anatomic site and histotypes of the primary lung cancer are reported in Supplementary Material (Section S1).

All patients underwent ^{18}F-FDG PET/CT. Overall, we analyzed 28 primary lung cancers (patients #1, #3 and #6 had two primary lung cancers, patients #11, #16 and #17 had three primary lung cancers) and 11 biopsy-proven metastatic lymph-nodes characterized by moderate/intense ^{18}F-FDG uptake. Regarding the histological classification, we analyzed 22 adenocarcinomas and 6 other histotypes.

2.2. ^{18}F-FDG PET-CT acquisition protocol and data reconstruction

All patients (6 h fasting-state, blood glucose levels <150 mg/dl) underwent dynamic PET acquisition using an integrated PET-CT scanner (Biograph mCT, Siemens Healthcare), with a low-dose unenhanced CT (120 kV, 90 mA) performed over the thoracic region with a field-of-view of 21 cm. The *trans*-axial CT matrix size was 512x512 (1 mm × 1 mm x 3 mm). A mean of 240 MBq of ^{18}F-FDG (range: 185–333 MBq, according to the body mass index) were intravenous injected (10 ml infusion of ^{18}F-FDG at a rate of 4.32 ml/s followed by a 10 ml saline flush) using an infusion pump (TemaSinergie, model RADInject). The actual dose delivered to the patient was calculated accounting for the residual activity in the infusion system.

PET images were acquired in list mode over the same area defined at low-dose CT, lasting 60 min. Dynamic PET frames were defined and reconstructed according to previously reported protocol [33]: 24 frames at 5 s, 12 frames at 15 s, and 11 frames at 300 s. Each frame was reconstructed with the OSEM algorithm, including time-of-flight and Ultra HD recovery with 21 subsets and 2 iterations, with *trans*-axial PET matrix size of 256x256 (3.18 mm × 3.18 mm x 3 mm). After dynamic acquisition, whole-body PET-CT was acquired and images were reconstructed using the protocol described above [33]. CT images were used for attenuation correction, anatomical localization, and fusion with PET images (Syntegra software, Siemens).

2.3. Kinetics of ^{18}FDG uptake of adenocarcinoma and other tumors

The purpose of the ML-based method we are going to develop is the automated classification of AD, the most common type of lung cancer, and other histotypes of tumors, which are from now on classified as NAD (*not-adenocarcinoma*). In Fig. 1A, a representative PET image overlaid to

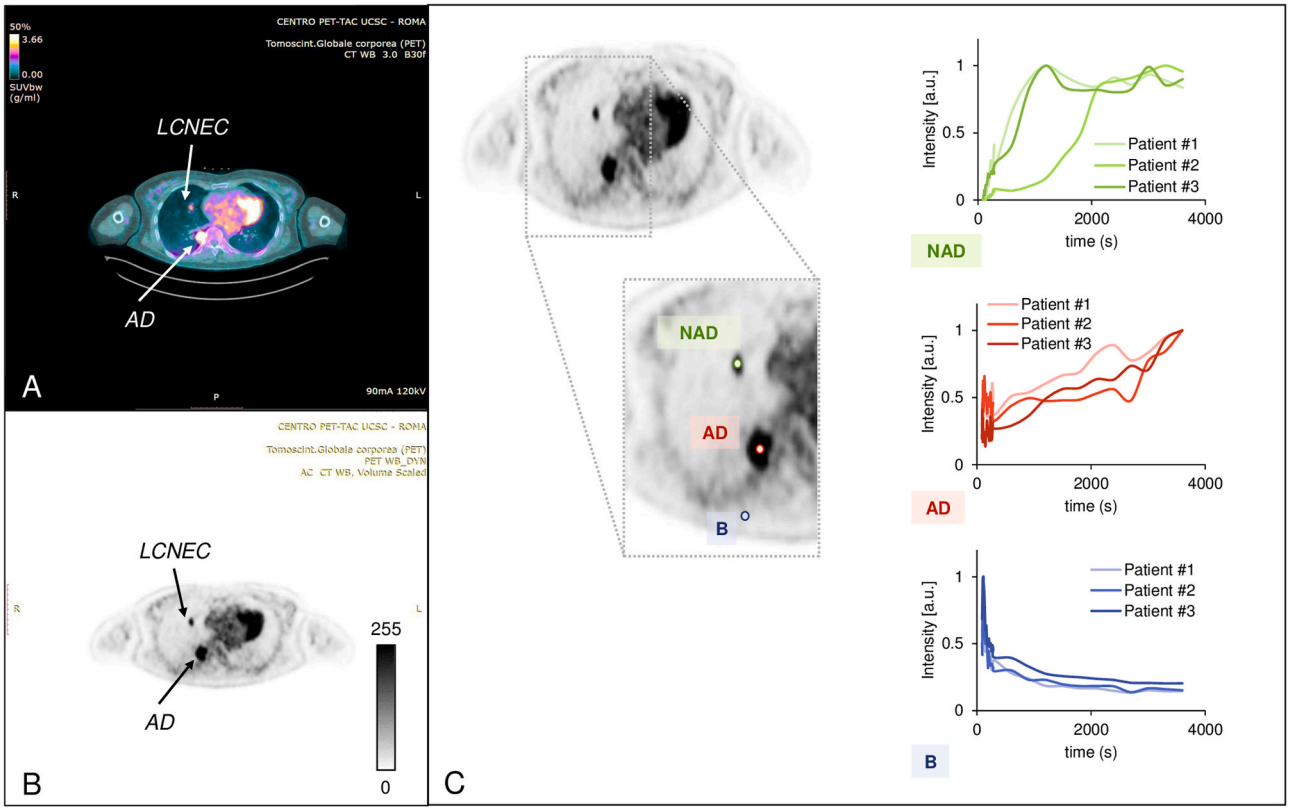

Fig. 1. Kinetics of ^{18}F-FDG uptake of adenocarcinoma and large cell neuroendocrine carcinoma. (A) Overlay of PET-CT image, represented in a color-coded scale from green to yellow with increasing the ^{18}F-FDG uptake. (B) Emission intensity of adenocarcinoma (AD) and large cell neuroendocrine carcinoma (LCNEC), represented in a grayscale (low intensity, white = 0; high intensity, black = 255). (C) Different kinetics of ^{18}F-FDG uptake for AD, NAD, and background (B). The three graphs represent the emission intensity of AD (red), NAD (green), and B (blue) as a function of the acquisition time for three different patients. The criterion used for voxels' selection is highlighted in the magnification of the image.

the CT image is reported in a color-coded scale ranging from green to yellow, while in Fig. 1B, only the PET image is reported in grayscale. In this representative image, two different histotypes are present: AD and LCNEC, which is therefore classified as NAD. Both AD and LCNEC are yellow-colored in Fig. 1A and black-colored in Fig. 1B. This image shows that both lesions, regardless their histotypes, are characterized by a higher uptake than the surrounding. After the evaluation of the normalized emission intensity ($I_{norm} = I/I_{max}$) of a subset (n = 5) of analyzed samples taken from different patients, 1 h after ^{18}F-FDG administration, we performed an unpaired two-sided *t*-test to evaluate if the intensity statistically differs between the two histotypes. The result of this analysis, giving a p-value > 0.05, highlights that no significant differences can be retrieved between AD (0.946 ± 0.065) and NAD (0.873 ± 0.217). This means that, relying only on the intensity of the image, it is not possible to distinguish between the two histotypes.

However, although characterized by the same ^{18}F-FDG-uptake, Fig. 1C shows that AD show different uptake kinetics with respect to NAD tumors. In the graphs, the emission intensity (y-axis, arbitrary units) for AD (red), NAD histotypes (green) and background (blue) is reported as a function of the time of image acquisition after tracer's administration (x-axis, expressed in seconds). Representative ^{18}F-FDG uptake curves are reported for three different patients, and voxels corresponding to each class are highlighted in the magnification of the image. Looking at these kinetics, it is possible to observe that no ^{18}F-FDG uptake occurs in the background, constituted by healthy tissues and/or organs, while tumors show a high ^{18}F-FDG demand, regardless their histotypes. However, while the AD kinetics are characterized by a slight, slower uptake, NAD tumors are characterized by a fast, steep ascent followed by the attainment of a saturation level, reached ~1000 s after the ^{18}F-FDG infusion. These observations, although interesting to highlight macroscopic differences between the AD and NAD kinetics, are indicative. No statistical analysis was performed, and curves were not parametrized since we will rely on a model-free approach which will be described in the following sections.

2.4. Workflow for the classification of AD and NAD tumors on dynamic PET imaging data

The scheme of the workflow for the ML-based method to classify tumors according to their histotypes is represented in Fig. 2.

The workflow is divided in five steps and can be implemented by using the open-source software Ilastik [34] and the open-source image processing tool ImageJ (NIH).

1) *Building of the time-resolved dPET stack (software: ImageJ).* Since the classification workflow relies on the kinetic of tracer uptake to classify and localize different tumors, we considered only the PET slice corresponding to the z-plane containing the tumor (see Section S2, Supplementary Materials), as per the contouring provided by the physician, to build the stack representing the temporal sequence of radionuclide tracer uptake, which consisted of 47 time-frames with resolution 512×512 voxels (Step 1). Each time frame is treated as an additional image channel for the next Step 2. In this way, we created "artificial" color channels for the learning algorithm, introducing an original data structure in which the statistical unit object of learning, rather than a single 2D-pixel (x,y), is a set of voxels with 2+n dimensions (x, y, t_1, t_2, …, t_n). For the training of the classifier, we used pixels from dPET stacks of 22 tumors (17 AD and 5 NAD histotypes) out of 28 tumors, corresponding to the 78%, that were provided as an

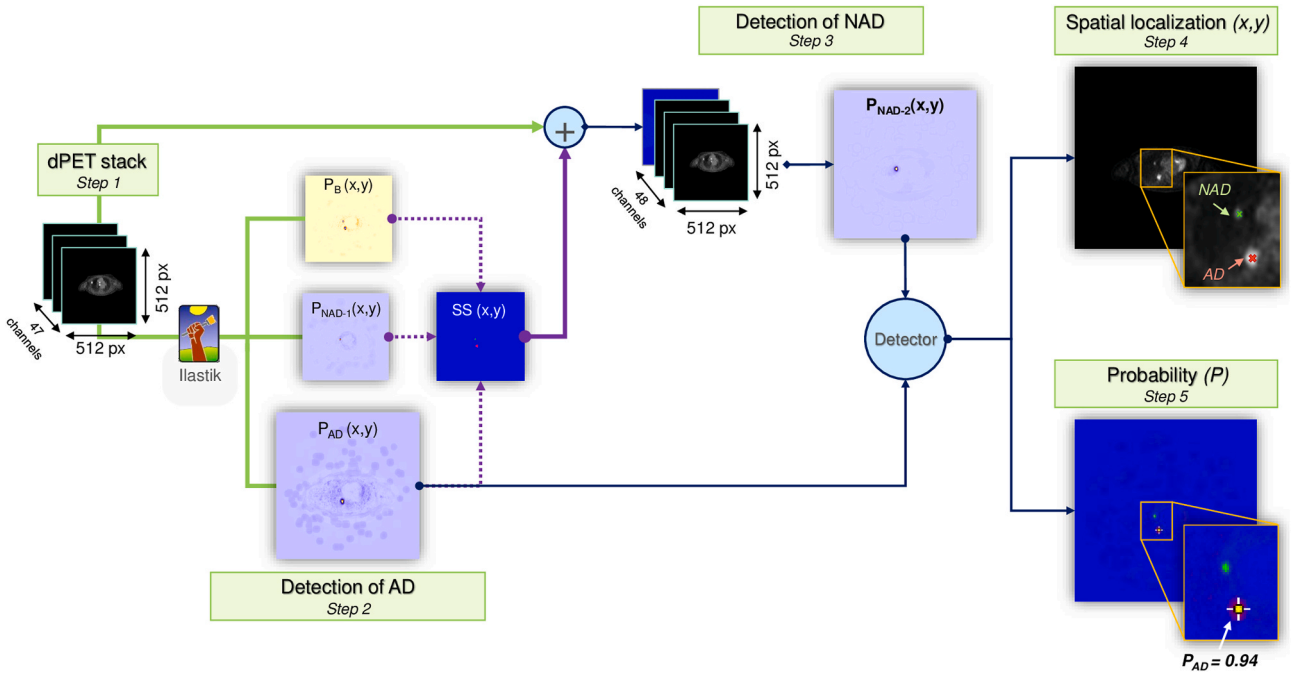

Fig. 2. Workflow for the ML-based method for classification of different histotypes of tumors. The workflow represented consists in five major steps. Step 1: construction of the time-resolved stacks for tumors (adenocarcinomas and other histotypes). Step 2: first-stage voxel-classification through the open-source software Ilastik, providing the detection of adenocarcinomas. In this first level, three classes were defined: adenocarcinoma (AD), not-adenocarcinoma (NAD) and background (B). The output consists in a probability map for each class ($P_{AD}(x,y)$, $P_{NAD-1}(x,y)$ and $P_B(x,y)$, respectively). The merge of the three probability maps provided the semantic segmentation (SS) image, which was added to the original stack and used as input for the second-stage of classification (Step 3), which is based on the same voxel-classification approach and allows for the detection of other tumor histotypes. The probability maps obtained for AD in Step 2 and for NAD in Step 3, respectively, constituted the input for the detector, that is finally able to provide both the spatial localization of adenocarcinomas and not-adenocarcinomas (Step 4) and to assign a probability value of belonging to a specific class to each voxel of the image (Step 5).

input for the Step 2. The remaining 6 stacks (22%) were used as test set to measure the performance of the technique.

2) *Detection of adenocarcinoma (software: Ilastik).* Voxel-classification workflow assigns labels to voxels based on spatial features and user annotations. This workflow employs by default a Random Forest classifier, a flexible supervised learning algorithm which builds multiple decision trees and merges them together to get more accurate and stable predictions [35,36]. To train the Random Forest classifier, dPET stacks of 22 tumors out of 28 tumors (78%) are used. Three classes are defined in the first stage, according to the different kinetics of uptake of ^{18}F-FDG: B, background; AD, adenocarcinomas and NAD, other histotypes. The software provides the following feature types:
   - Color/Intensity, that use color or brightness to discern objects;
   - Edge, accounting for brightness or color gradients to discern objects;
   - Texture, an important feature if the objects in the image have a special textural appearance.

For image classification we select the following spatial features, calculated on each of the 47 image channels representing a time step: Gaussian Smoothing for Color/Intensity, Laplacian of Gaussian, Gaussian Gradient Magnitude and Difference of Gaussians for Edge, and Structure Tensor Eigenvalues and Hessian of Gaussian Eigenvalues for Texture. A detailed description of features properties is reported in Section S3 (Supplementary Materials). Usually, when semantic segmentation is performed on PET or other medical physics images, only texture features or features detecting brightness and brightness gradients are used, since in this context we deal only with grayscale images. In this workflow, since the images are characterized by n-additional channels which are the dPET images acquired at different times, we can exploit color brightness and gradient features due to temporal differences related to the distinct kinetics of uptake. For this reason, it is important to consider color information, as well as brightness gradients and texture features, to uncover those relations and correlations between voxels that are embedded in the time evolution of tracer uptake.

For each class, a probability map (single channel image, 512 × 512 voxels resolution, 32-Bit), representing the probability that each voxel belongs to the selected class ($P_B(x,y)$, $P_{NAD-1}(x,y)$ and $P_{AD}(x,y)$, respectively), is obtained. It holds the normalization condition $P_B(x,y)+P_{NAD-1}(x,y)+P_{AD}(x,y) = 1$ for each voxel (x,y). The probability map $P_{AD}(x,y)$ serves as a first input for the automated detector used for the spatial localization and the quantification of probability.

The probability maps provides the rationale to build the semantic segmentation image ($SS(x,y)$), consisting in a single channel image (512 × 512 voxels resolution) with three values, each corresponding to one class. The class is obtained by selecting the maximum element of $P_B(x,y)$, $P_{NAD-1}(x,y)$ and $P_{AD}(x,y)$ at each voxel. This image, in combination with the dataset built in Step 1, constitutes the input for the detection of NAD tumors (Step 3).

3) *Detection of other tumor (software: Ilastik).* To ultimately distinguish tumor histotype, the 'Autocontext' approach is applied. Although from the first stage of voxel-classification it is possible to distinguish the three probability maps, the application of this procedure is particularly efficient and highly recommended when the image data show multiple distinct classes since it improves the voxel-classification workflow by training a cascade of classifiers. Indeed, a better accuracy is guaranteed, and observed from a comparison of the probability values obtained for the class of other tumor from the first and second stage, respectively, by the fact the segmented image obtained in the previous stage is added as new channel to the raw data. The input of this second-stage segmentation thus consists in a 48-channels stack, obtained by adding the *SS* image to the dPET data

generated in Step 1. The algorithm of 'Autocontext' is optimized to compute features on these results, meaning that it can then learn to interpret edges and texture variations in probability maps as well as in the raw data. A detailed description of this workflow is reported in [37]. For this second stage, only two classes are defined: other tumor and background. The probability map ($P_{NAD\text{-}2}(x,y)$) obtained as the output of this second stage, combined with the $P_{AD}(x,y)$ previously obtained from Step 2, is used as the second input for the automated detector.

4) *Spatial Localization (x,y).* The histotype class of different tumors is classified relying on the probability maps P_{AD} and $P_{NAD\text{-}2}$, analyzed using the open-source software ImageJ (NIH), according to the workflow described in the previous steps. To provide for a spatial localization of AD and/or NAD tumors, the 'Find Maxima' tool (ImageJ) is applied. To filter non-meaningful multiple local maxima that can be due to noise fluctuations, we set the algorithm by imposing to ignore local maxima if their value does not emerge from the surroundings by more than a defined value, called 'prominence', which was set to 0.5 for our dataset. By applying this method, we ensure that a single point, corresponding to the maximum above prominence, is identified and highlighted for each region characterized by a higher probability value than the surrounding, thus avoiding the requirement for average calculations that can be affected by the arbitrary selection of the voxels belonging to the tumor. This procedure is applied to both P_{AD} and $P_{NAD\text{-}2}$ to identify voxels classified as adenocarcinomas and those classified as other histotypes. According to this choice, all the maxima above the prominence threshold set were, then, marked by a red cross if they are classified as adenocarcinomas and by a green cross if they are classified as other tumors, respectively, and the result of this localization consists in a couple of coordinates (x,y) which was overlaid to the original PET image, to assess the correspondence between both the histotype and the position defined by the classifier and that provided by the physician.

5) *Probability (P).* The last step of the workflow for tumor classification consists in obtaining, for each voxel of the image, the probability value, and the corresponding uncertainty, of belonging to a specific histotype class (AD or NAD tumor). These values, combined with the coordinates provided by Step 4 and then collected in a table, will provide a prediction of both the histological and spatial characterization of the detected lesions.

2.5. Statistics

Statistical T-tests for sets of biological/biophysical data are performed by the free software environment R (https://www.r-project.org/, Version 4.1.2). Baseline characteristics among groups have been compared with ANOVA for parametric variables and p-values below 0.05 ($p < 0.05$) were considered statistically significant.

3. Results

3.1. Automated detection of tumors: classification of tumor histotypes

The results of the detection of AD and NAD tumors, with the output of the classification, the associated probability value, the corresponding uncertainty, and the spatial position (x,y) are summarized in Table 1. The number of the detected lesions is reported in the second column for each patient, along with their histotype (third column). A total of 28 tumors was included in the study, including 8 non-small cells lung carcinoma favoring adenocarcinoma (NSCLC, 28.6%), 14 adenocarcinomas (AD, 50.0%), 2 large cell neuroendocrine carcinoma (LCNEC, 7.1%) and 4 squamous cell carcinoma (SqCC, 14.3%). However, for the automated detection and classification, tumors are divided in 22 AD, including NSCLC and AD, and 6 NAD, including LCNEC and SqCC, according to the different kinetics of ^{18}F-FDG uptake, and the output of the classifier is reported in the fourth column. By comparing the different tumors' histotypes known from the existing biopsy diagnosis, that constitute the gold-standard against which the model is trained, with the

Table 1
Output of the classification of tumor histotypes. The table reports the characteristics of the tumors considered for this study: the histotype, as provided by the histologic examination (AD = adenocarcinoma; NSCLC = non-small cell lung carcinoma (favouring AD); LCNEC = large cell neuroendocrine carcinoma; SqCC = squamous cell carcinoma), the output of the classifier (AD = adenocarcinoma; NAD = other histotype), the probability value associated to the defined class along with the corresponding k of the cross-validated procedure, the relative uncertainty, the voxel position of the detected lesion (x,y) and the index of localization ε.

Patient	# Tumors	Histotype	Classification Output	Probability	k	Uncertainty	X (voxel)	Y (voxel)	ε
#1	01T	NSCLC	AD	0.98	2	0	97	121	0.02
	02T			0.64	1	0	109	141	0.33
#2	01T	NSCLC	AD	0.2	3	0.13	115	152	0.59
#3	01T	AD	AD	0.9	2	0.12	119	157	0.29
	02T	LCNEC	NAD	0.96	3	0	112	136	0.30
#4	01T	NSCLC	AD	0.57	3	0	108	140	0.31
#5	01T	AD	AD	0.79	2	0	153	120	0.15
#6	01T	AD	AD	0.91	1	0	157	135	0.59
	02T			0.99	3	0	161	136	0.34
#7	01T	LCNEC	NAD	0.83	1	0	93	142	0.49
#8	01T	NSCLC	AD	0.54	2	0.02	110	118	0.36
#9	01T	AD	AD	0.94	3	0.1	106	138	0.35
#10	01T	NSCLC	AD	0.99	3	0	160	141	0.41
#11	01T	AD	AD	0.78	1	0	131	128	0.81
	02T			0.99	1	0.02	98	132	0.47
	03T			0.83	2	0.04	104	143	0.26
#12	01T	SqCC	NAD	1	2	0	165	136	0.74
#13	01T	NSCLC	AD	0.56	3	0	158	128	0.40
#14	01T	AD	AD	0.83	1	0.34	112	149	0.69
#15	01T	AD	AD	0.72	3	0	104	183	0.29
#16	01T	SqCC	NAD	1	1	0	107	140	0.79
	02T			0.69	1	0	118	146	0.65
	03T			0.54	2	0	92	134	0.42
#17	01T	AD	AD	0.8	1	0.4	104	118	0.40
	02T			0.1	3	0.12	149	116	0.34
	03T			0.95	1	0.08	142	139	0.14
#18	01T	NSCLC	AD	0.25	2	0	104	135	0.39
#19	01T	AD	AD	0.5	3	0	143	146	0.64

classification output, it is possible to observe that the classifier can distinguish adenocarcinomas from other histotypes of tumors in all the evaluated cases.

The probability maps obtained following the workflow previously described (see Section 2.5) associate a probability value at each tumor detected and classified, as reported in the Probability column in Table 1. This value, extracted from P_{AD} (x,y) or $P_{NAD\text{-}2}$ (x,y) depending on the classification output provided by the classifier, ranges from 0 (lowest probability, surely not belonging to the specific class) to 1 (maximum probability, surely belonging to the class). To check the strength of the method and to exclude any arbitrary dependence on the chosen training and test sets, respectively, we applied a k-fold cross-validation strategy with k = 3, by changing the tumors used for training the classifier and those used to evaluate its performance, while keeping fixed the same relationship between them. The mean probability values for tumors belonging to the test set are reported in Table 1 along with the corresponding k of the cross-validation procedure. By applying this method, we calculated the mean probability associated to AD and that associated to NAD, obtaining 0.704 ± 0.268 for AD, and 0.948 ± 0.189 for NAD, respectively. This result allows us to observe that the classifier not only localizes tumors, but it also discriminates the histological type of lesion. To quantify the ability of the k-fold cross-validated procedure applied in discriminating the different histotypes, we evaluated the accuracy of this strategy and compared it with the overall accuracy of the non-cross-validated approach. Calculating the ratio of the properly classified tumors over the total tumors included in the test set, we obtained accuracy values of 83% for the non-cross-validated method, and of 89% for the k-fold cross-validation strategy. The accuracy reported for the k-fold validation strategy is the mean obtained by averaging the single accuracies retrieved for each fold of the procedure, 100% for k = 1, 88% for k = 2, and 80% for k = 3, respectively. Considering these values, a 10% standard deviation should be associated to the 89% accuracy reported. This result, besides confirming the high accuracy of the described classification tool, also highlights that the application of the k-fold cross-validation ensures an improvement in the histotypes identification.

However, since the Random Forest classifier consists of many decision trees ($N_T = 100$), and each pixel is classified by collecting the votes of each individual tree, besides the prediction maps, the software also computes an uncertainty map, by associating at each pixel the value obtained by subtracting the two highest votes attributed to different classes (H_{V1} for class 1, and H_{V2} for class 2, respectively) (H_{V1} and H_{V2}, respectively) at that pixel, and subtracting that from 1, according to the following equation

$$uncert = 1 - (H_{V1} - H_{V2})$$

An uncertainty map is generated for each stage of the classification workflow, meaning that, at the end of the two-stage pixel classification, we obtained two uncertainty maps. To properly associate at each pixel the uncertainty corresponding to the used classified, we followed the procedure described in detail in Section S4 (Supplementary Materials). The uncertainty values associated to each lesion also provide a measure for the accuracy of the workflow. The mean uncertainty associated to detection of adenocarcinoma is 0.069, while for other tumors is approximately 0.

In addition, to evaluate the correspondence between the position defined by the classifier and that provided by the physician, we associated to each tumor an index of localization ε. This index, reported in the last column of Table 1, was calculated according to the following formula:

$$\varepsilon = \frac{\Delta CM}{R}$$

where ΔCM is the distance between the center of mass of the detected area (CM_{tumor}) and the center of mass of the area highlighted by the physician (CM_{ROI}), calculated as

$$\Delta CM = \sqrt{(x_{CM_{tumor}} - x_{CM_{ROI}})^2 + (y_{CM_{tumor}} - y_{CM_{ROI}})^2}$$

If the index of localization ε is lower than 1, it indicates a correct localization, otherwise it provides a measure of the misclassification. The mean value of this error (0.49 ± 0.20) confirms the power of the localization tool.

A more detailed explanation of how the index is calculated is reported in Section S5 (Supplementary Materials.

3.2. Estimation of the lymph-node metastatic risk

The process based on voxel-classification provides, as an output, the probability associated with each voxel in the image of belonging to the adenocarcinoma class rather than the other. Moreover, the application of the whole workflow for the detection and automatic classification of the different tumor histotypes previously described detects the spatial position of the regions characterized by highest probability values. The analysis of the probability maps and the results provided by the detector revealed the presence of local maxima in correspondence of the lymph-nodes, thus highlighting the existence of regions characterized by a ^{18}F-FDG uptake that falls with high probability in the AD class.

In Fig. 3, the automated detection of lymph nodal regions with adenocarcinoma-like ^{18}F-FDG uptake is shown. In Fig. 3A a single PET image collected 1 h after ^{18}F-FDG administration is represented in grayscale, with intensity values ranging from 0, corresponding to low intensity, i.e., low ^{18}F-FDG uptake (white), to 1, high intensity that is increased ^{18}F-FDG uptake (black). Four dark regions can be easily identified: two corresponding to tumors and indicated as 02T and 03T, respectively, and two corresponding to lymph-nodes, indicated as 01N1 and 01N2. While the histotype of both the tumors is known (adenocarcinomas), to obtain histological information is not always feasible for lymph-nodes.

Looking at this intensity-based picture, in which all the regions with an increased ^{18}F-FDG uptake are dark, it is not possible to distinguish tumors from other non-neoplastic tissues with a high ^{18}F-FDG demand and, moreover, no information about the different kinetics can be retrieved. However, the AD probability map (P_{AD}) represented in Fig. 3B in a color-coded scale ranging from light purple (probability = 0) to yellow (probability = 1) revealed the presence of yellow-colored regions (i.e. high probability regions) that, although other than tumors, are characterized by a high probability of belonging to the AD class. The local maxima identified by the automated workflow for tumor detection and classification are indicated by the green dots shown in Fig. 3B and highlighted in the magnification, where they are labelled according to their nature (02T and 03T, tumors; 01N1, lymph-node). The red dashed line was used to evaluate the profile of the probability and the corresponding distance in voxels (from 0 to 50) is indicated in the picture. In Fig. 3C, the plot profile of the probability value of being adenocarcinoma (y-axis) is reported as a function of the distance in voxels (x-axis). The graph shows that not only tumors but also one of the two lymph-nodes (01N1) is characterized by a high probability value ($P_{AD} > 0.05$, dashed black line) of belonging to the AD class, thus identifying a lymphatic region characterized by an increased ^{18}F-FDG uptake, similar to that of the adenocarcinoma.

Following this observation, we evaluated the probability value of belonging to the class of adenocarcinoma, associated by the classifier to each lymph-node identified by the physician. A summary of all the lymph-nodes, with the result of the histological exam (when available), the associated AD-probability value, the corresponding uncertainty, and the spatial position (x,y) are reported in the following Table 2.

Histological evidence of metastatic nature was available in 11/47 visually PET-positive lymph-nodes. Since the classifier was trained on voxels characterized by the ^{18}F-FDG uptake of adenocarcinomas, a high probability value associate to lymph-nodes can be considered as representative of an increased metabolic activity similar to that of tumors

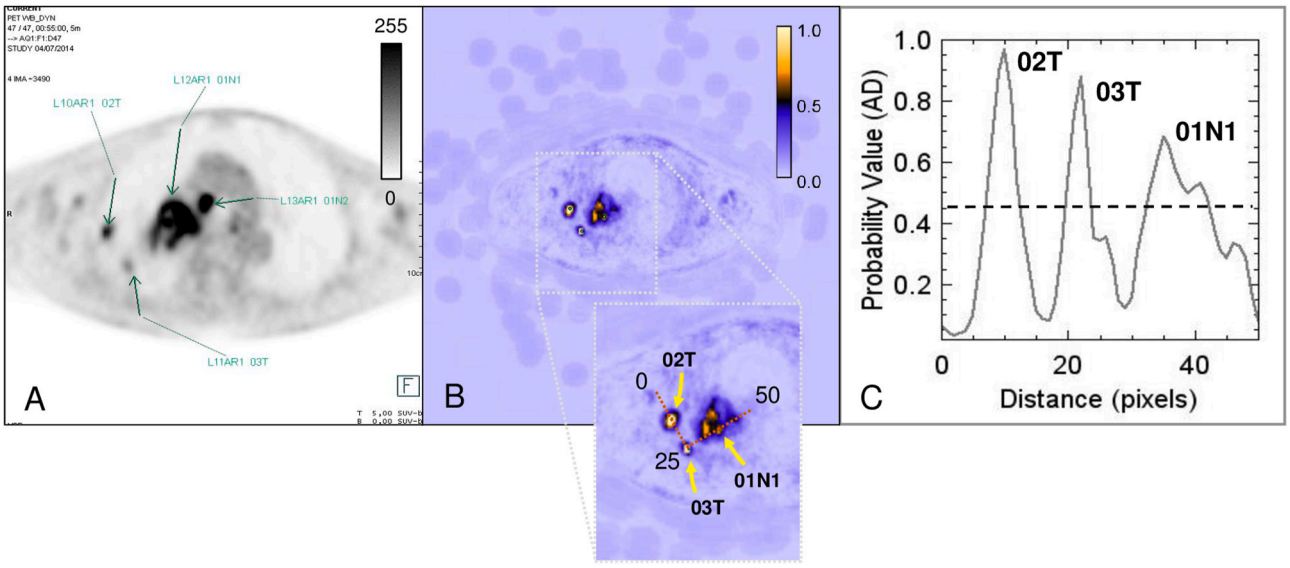

Fig. 3. Detection of lymph nodal regions with AD-like FDG uptake. (A) Single PET image represented in grayscale (0 = low intensity, white; 1 = high intensity, black) showing two tumors (02T and 03T, both adenocarcinomas) and two lymph-nodes (01N1 and 01N2, without histological indication). (B) Adenocarcinoma probability map P_{AD} (x,y). Each voxel's color spans from light purple (probability = 0) to yellow (probability = 1). The yellow-colored regions, indicated by the green dots, are highlighted in the magnification reported along with the probability map, and labelled according to their nature (02T and 03T, tumors; 01N1, lymph-node). The dashed line is used to evaluate the profile of the probability and the corresponding distance in voxels is indicated. (C) Plot profile of the probability value of being adenocarcinomas (y-axis) as a function of distance (in voxels, x-axis) obtained for tumors and lymph-node. The graph shows that not only tumors but also one of the two lymph-nodes (01N1) are characterized by a high probability value ($P_{AD} > 0.5$, dashed black line) of belonging to the AD class.

and, therefore, of a metastatic risk probability.

Looking at the values reported in Table 2, it is possible to observe that 6 of the 11 confirmed metastatic lymph-nodes, corresponding to 54.5%, are classified as AD with a probability value higher than 0.5. In this perspective, to quantify the extent of the informative content of the uptake kinetics for predicting lymph-node metastatic nature, we divided the probability values assigned to voxels corresponding to lymph-nodes in fourth quartiles: Q1, for probability values between 0% and 24.9%; Q2, probability between 25% and 49.9%; Q3, probability between 50% and 74.9% and Q4, probability between 75% and 100%.

The results of the quartile distribution analysis of lymph-nodes are reported in Table 3. While the first and second column summarizes the range of percentages that characterizes each quartile, the number of identified lymph-nodes belonging to each Q-interval is reported in the third column. According to the trained classifier for tumors histotypes detection and classification, 34 lymph-nodes were associated with a probability of belonging to the AD class lower than 50% (in particular, 19 lymph-nodes have a probability lower than 25% (Q1), and 15 a probability between 25% and 49.9% (Q2)), while 13 were classified as AD with a probability higher than 50% (11 lymph-nodes between 50% and 74.9% (Q3) and 2 lymph-nodes with a probability higher than 75% (Q4)). The total number of visually PET-positive nodes included in the analysis (47) is reported in the last line, in bold. The result obtained from the classifier was, therefore, compared with the known outcome of the available histological examination. The number of confirmed metastatic lymph-nodes belonging to each quartile range is reported in the fourth column: 2 of them, though metastatic, were associated with a probability value lower than 25%, 3 with a probability between 25% and 50%, 4 with a probability between 50% and 75% and 2 with a probability higher than 75%. To estimate the ability of the classifier in predicting the risk of metastasis associated with lymph-nodes, we then assessed the fraction of truly metastatic lymph-nodes attributed to the different quartiles with respect to the total number of lymph-nodes belonging to each interval, according to the following formula $predictive\ accuracy = \frac{metastatic\ nodes}{\#\ nodes}$. The value of predictive accuracy is reported in the fifth column of Table 3. The percentages retrieved, from 11% for Q1 to 100% for Q4, through the 20% and 36% for Q2 and Q3, respectively, revealed that in each quartile the fraction of metastatic lymph-nodes identified increases, thus indicating how probability values higher than 50% of belonging to the adenocarcinoma class are with good accuracy associated with metastatic lymph-nodes. Further considerations on the power of this application are reported in Section S6 (Supplementary Materials).

4. Discussion and conclusions

In recent years, due to the improvement of imaging data acquisition techniques, the increasing number of large datasets and the urgent need for more accurate and precise analysis tools, ML-based approaches have received growing attention [10,38]. Among them, the supervised semantic segmentation, referring to a process of assigning a semantic label to each voxel of an image, has been extensively used for bioimage analysis [39]. However, since semantic segmentation classifies voxels according to their features, one of the main challenges of this kind of approach is that classes characterized by a high degree of similarity in visual appearance can in principle reduce the ability of the classifier to discriminate properly. The potential limit of this approach emerges also in the analysis of PET images, where the increased glucose uptake of different types of tumors or again structures other than tumors (i.e., lymph-nodes) can affect the correct detection of pathological/neoplastic lesions. However, the information provided by the dynamic PET data acquisition on the time-resolved ^{18}F-FDG uptake, which is contained in each voxel, can constitute the additional key feature that allows discriminating between the different histotypes of tumors, lymph-nodes, and other non-neoplastic tissues. The hereby presented application of a multi-stage voxel classification provide an accurate semantic image segmentation, identifying and classifying the regions of the image according to a combined approach combining spatial features and uptake kinetic. This has resulted in the definition of a workflow for the automated detection and classification of AD and NAD on dynamic PET imaging data through machine-learning driven semantic segmentation. With respect to previous methods and to the use of single-image, non-dynamic PET data [23–25,40], this algorithm presents improved performances. The ML method, relying contextually on several ^{18}F-FDG uptake spatial and temporal features, generates as an outcome

Table 2
Evaluation of the metastatic probability for detected lymph-nodes. The table reports the characteristics of the lymph-nodes for each patients: the histotype (when determined) as provided by the histologic examination (metastatic = malignancy confirmed), the metastatic probability value associated to each lymph-node, the corresponding uncertainty and the voxel position of the detected node (x,y).

Patient	# PET positive lymph-nodes	Histotype	Metastatic Probability	Uncertainty	X (voxel)	Y (voxel)
#1	01N2	*not defined*	0.01	0.02	123	119
	02N2	*not defined*	0.12	0.00	124	129
#2	01N1	*not defined*	0.04	0.00	115	141
#3						
#4	01N1	**metastatic**	**0.78**	0.39	117	132
	02N1	**metastatic**	**0.79**	0.38	112	130
#5						
#6	01N1	*not defined*	0.14	0.00	151	135
	01N2	*not defined*	0.16	0.00	141	131
	02N1	*not defined*	0.19	0.00	149	137
#7						
#8	01N1	**metastatic**	**0.52**	0.94	110	119
#9	01N1	**metastatic**	**0.06**	0.00	115	140
#10	01N1	*not defined*	0.29	0.00	150	134
	01N2	*not defined*	0.21	0.42	138	133
	02N2	*not defined*	0.21	0.00	128	133
	03N2	*not defined*	0.33	0.00	137	122
	04N2	*not defined*	0.18	0.00	134	125
#11	01N1	*not defined*	0.31	0.00	118	127
	01N2	*not defined*	0.05	0.00	125	124
	01N3	*not defined*	0.01	0.02	111	119
	02N1	*not defined*	0.03	0.06	118	128
	02N2	*not defined*	0.18	0.00	124	126
#12						
#13	01N2	**metastatic**	**0.43**	0.89	137	125
	02N2	**metastatic**	**0.68**	0.00	134	117
	03N2	**metastatic**	**0.28**	0.58	136	124
	04N2	**metastatic**	**0.69**	0.61	145	135
	05N2	**metastatic**	**0.51**	0.00	141	129
#14						
#15	01N1	**metastatic**	**0.27**	0.00	117	166
	01N2	**metastatic**	**0.05**	0.00	130	163
#16						
#17						
#18	01N1	*not defined*	0.12	0.24	118	129
#19	01N1	*not defined*	0.55	0.88	128	129
	02N1	*not defined*	0.54	0.91	140	131
	01N2	*not defined*	0.59	0.82	131	112
	02N2	*not defined*	0.47	0.95	131	128
	03N2	*not defined*	0.28	0.62	133	126
	04N2	*not defined*	0.32	0.67	135	116
	05N2	*not defined*	0.30	0.65	135	119
	06N2	*not defined*	0.48	0.99	132	126
	07N2	*not defined*	0.73	0.53	138	127
	08N2	*not defined*	0.66	0.65	142	126
	09N2	*not defined*	0.58	0.82	128	130
	10N2	*not defined*	0.23	0.48	135	127
	11N2	*not defined*	0.12	0.26	141	133
	12N2	*not defined*	0.63	0.71	142	126
	13N2	*not defined*	0.30	0.66	137	121
	14N2	*not defined*	0.36	0.74	126	132
	01N3	*not defined*	0.45	0.92	122	121
	02N3	*not defined*	0.14	0.30	124	121
	03N3	*not defined*	0.43	0.65	135	119

probability map allowing to distinguish AD from NAD tumors, ultimately increasing the specificity of the technique. Indeed, the relevance of this approach relies in the fact that time stacks are used to perform machine learning based pixel classification. The creation of "artificial" color channels, corresponding to the different time points, allows to exploit, besides brightness gradients and texture, also color features and gradients, corresponding in our picture to time features and gradients (i.e. kinetics) for the tumors classification. This constitutes a powerful improvement in pixel classification, since it allows to exploit an easy-to-use tool to uncover those relations and correlations between voxels, that are embedded in the time evolution of tracer uptake. For this reason, the use of the developed algorithm guarantees an automatic and more accurate localization and discrimination of tumors, providing, as output of the classification, not only the spatial position (x,y), but also the associated probability value, with the corresponding uncertainty (0.943 ± 0.093, for AD, and 0.958 ± 0.090, for NAD, respectively).

Another important aspect of this tool is the assistance they can furnish in detecting at which extent tumor has spread beyond the primary lesion into lymphatic system. In this pilot study, the developed algorithm has successfully recognized if lymph-nodes were affected by tumor spreading, with a well-defined value of probability and uncertainty. Indeed, among the 11 confirmed metastatic lymph nodes, 6 were classified as belonging to the adenocarcinoma class with a probability value higher than 50%, 3 with probability between 25% and 50% and 2 with a probability lower than 25%. These preliminary results pave the way for further optimization and validation of the algorithm for extending its use well beyond adenocarcinoma classification, through a well-planned longitudinal study, with the aim of providing the physician

Table 3
Quartile distribution of metastatic lymph-nodes. The table reports the probability associated to lymph-nodes divided in fourth quartiles: Q1, probability from 0% to 24.9%; Q2, probability from 25% to 49.9%; Q3, probability from 50% to 74.9%; Q4, probability from 75% to 100%. The number of lymph-nodes belonging to each quartile is reported in the third column, while the fourth column indicates the number of confirmed metastatic lymph-nodes included in each range (the sum of lymph-nodes is reported in the last line, in bold). The fifth column corresponds to the percentage of metastatic nodes belonging to each quartile with respect to the total number of lymph-nodes included in Q1, Q2, Q3 and Q4, respectively.

	quartiles range (%)	# nodes	metastatic nodes	
Q1	0–24.9	19	2	11%
Q2	25–49.9	15	3	20%
Q3	50–74.9	11	4	36%
Q4	75–100	2	2	100%
		47	**11**	

a preliminary picture of the general staging status of the patients.

Overall, this algorithm thus can speed-up and furnish further evidence in diagnosis and staging of lung cancer, which is undoubtedly a complex process. Diagnosing indeed includes not only categorizing lung cancers in ways that help to determine the best treatment plan, but also determining whether it has spread to other parts of the body. This method, in association with other tests, can thus help to decide which treatments might work best. This approach, being fully automated and completely independent of theoretical and experimental biases due to the definition and application of a mathematical model, and thus not requiring specific knowledge and skills from the user, is able to provide a very good indication of areas characterized by abnormal glucose uptake kinetics. Another advantage is that this technique relies to multiple PET acquisitions, improving the confidence in the evaluation and interpretation of dynamic PET/CT scans, thus mitigating misalignments of PET/CT images due to physiologic motions (e.g., cardiac and respiratory motions) [41,42]. Indeed, this workflow does not require an overlap between images acquired with a hybrid method. The overlap requires a standard calibration and alignment procedure which is user and machine dependent, and moreover since CT resolution is higher than the PET one, can suffer more deeply by physiological motions. A limitation of this study is the number of analyzed patients, that must be increased to optimize the protocol and the workflow. Moreover, since this ML-approach is based on the temporal information of glucose uptake contained in each voxel, it cannot disregard the acquisition of dynamic PET images, which requires a certain amount of time (~45 min) to be obtained. However, the definition of shorter acquisition protocols is feasible since the short dynamic acquisition immediately after tracer injection for the calculation of the input function can be neglected, being a model-free approach, and efforts can be concentrated in optimizing late dynamic acquisitions for improving the performance. In any case, especially for selected group of patients requiring a more accurate analysis, the dPET acquisition, combined with the application of this machine learning-based method for the semantic segmentation of dPET data, can be introduced in the clinical practice, by reserving ad-hoc slots especially at the beginning and at the end of the day. This step, together with the development of an automatized software, can be integrated in the clinical routine, providing a powerful tool to both support the physician in localizing area which need a deeper investigation and ensure early and accurate classification of tumors and metastatic lymph-nodes. Moreover, this tool, by exploiting specially optimized neural networks [43], can be potentially applied for the classification and organization of several types of data, including not only bioimages [44–46], but also text documents [47–49], and time-series [50], thus speeding up, favoring, and improving the analysis of even larger datasets.

Funding

This work was supported by Università Cattolica del Sacro Cuore Linea D1 2018 grant number R4124500391 (GM).

Declaration of competing interest

The authors declare that they have no known competing financial interests or personal relationships that could have appeared to influence the work reported in this paper.

Acknowledgments

The authors acknowledge the Cost Action CA15124 “NEUBIAS” for supporting training in image processing and analysis of GB.

Appendix A. Supplementary data

Supplementary data to this article can be found online at https://doi.org/10.1016/j.compbiomed.2022.105423.

References

[1] A. Zhu, D. Lee, H. Shim, Metabolic positron emission tomography imaging in cancer detection and therapy response, Semin. Oncol. 38 (2011) 55–69, https://doi.org/10.1053/j.seminoncol.2010.11.012.
[2] V. Kapoor, B.M. McCook, F.S. Torok, An introduction to PET-CT imaging, Radiographics 24 (2004) 523–543, https://doi.org/10.1148/rg.242025724.
[3] K. Vanhove, G.J. Graulus, L. Mesotten, M. Thomeer, E. Derveaux, J.P. Noben, W. Guedens, P. Adriaensens, The metabolic landscape of lung cancer: new insights in a disturbed glucose metabolism, Front. Oncol. 9 (2019), https://doi.org/10.3389/fonc.2019.01215.
[4] L. Schrevens, N. Lorent, C. Dooms, J. Vansteenkiste, The role of PET scan in diagnosis, staging, and management of non-small cell lung cancer, Oncol. 9 (2004) 633–643, https://doi.org/10.1634/theoncologist.9-6-633.
[5] J. Vansteenkiste, L. Crinò, C. Dooms, J.Y. Douillard, C. Faivre-Finn, E. Lim, G. Rocco, S. Senan, P. van Schil, G. Veronesi, R. Stahel, S. Peters, E. Felip, K. Kerr, B. Besse, W. Eberhardt, M. Edelman, T. Mok, K. O'Byrne, S. Novello, L. Bubendorf, A. Marchetti, P. Baas, M. Reck, K. Syrigos, L. Paz-Ares, E.F. Smit, P. Meldgaard, A. Adjei, M. Nicolson, W. Weder, D. de Ruysscher, C. le Pechoux, P. de Leyn, V. Westeel, 2nd ESMO consensus conference on lung cancer: early-stage non-small-cell lung cancer consensus on diagnosis, treatment and follow-up, Ann. Oncol. 25 (2014) 1462–1474, https://doi.org/10.1093/annonc/mdu089.
[6] H. Sung, J. Ferlay, R.L. Siegel, M. Laversanne, I. Soerjomataram, A. Jemal, F. Bray, Global cancer statistics 2020: GLOBOCAN estimates of incidence and mortality worldwide for 36 cancers in 185 countries, CA, A Cancer J. Clinic. 71 (2021) 209–249, https://doi.org/10.3322/CAAC.21660.
[7] J.Y. Song, Y.N. Lee, Y.S. Kim, S.G. Kim, S.J. Jin, J.M. Park, G.S. Choi, J.C. Chung, M.H. Lee, Y.H. Cho, M.H. Choi, D.C. Kim, H.J. Choi, J.H. Moon, S.H. Lee, S. W. Jeong, J.Y. Jang, H.S. Kim, B.S. Kim, Predictability of preoperative 18F-FDG PET for histopathological differentiation and early recurrence of primary malignant intrahepatic tumors, Nucl. Med. Commun. 36 (2015) 319–327, https://doi.org/10.1097/MNM.0000000000000254.
[8] M. Suárez-Piñera, J. Belda-Sanchis, A. Taus, A. Sánchez-Font, A. Mestre-Fusco, M. Jiménez, L. Pijuan, FDG PET-CT SUVmax and IASLC/ATS/ERS histologic classification: a new profile of lung adenocarcinoma with prognostic value, Am. J. Nucl. Med. Molecul. Imag. 8 (2018) 100. /pmc/articles/PMC5944825/. (Accessed 28 July 2021).
[9] A. Almuhaideb, N. Papathanasiou, J. Bomanji, 18F-FDG PET/CT imaging in oncology, Ann. Saudi Med. 31 (2011) 3–13, https://doi.org/10.4103/0256-4947.75771.
[10] K.P. Wong, D. Feng, S.R. Meikle, M.J. Fulham, Segmentation of dynamic PET images using cluster analysis, IEEE Trans. Nucl. Sci. 49 (2002) 200–207, https://doi.org/10.1109/TNS.2002.998752.
[11] I.R. Duffy, A.J. Boyle, N. Vasdev, Improving PET imaging acquisition and analysis with machine learning: a narrative review with focus on alzheimer's disease and oncology, Mol. Imag. 18 (2019) 1–11, https://doi.org/10.1177/1536012119869070.
[12] T. Wang, Y. Lei, Y. Fu, W.J. Curran, T. Liu, J.A. Nye, X. Yang, Machine learning in quantitative PET: a review of attenuation correction and low-count image reconstruction methods, Phys. Med. 76 (2020) 294–306, https://doi.org/10.1016/j.ejmp.2020.07.028.
[13] H. Arabi, A. AkhavanAllaf, A. Sanaat, I. Shiri, H. Zaidi, The promise of artificial intelligence and deep learning in PET and SPECT imaging, Phys. Med. 83 (2021) 122–137, https://doi.org/10.1016/j.ejmp.2021.03.008.
[14] L. Wei, I. El Naqa, Artificial intelligence for response evaluation with PET/CT, Semin. Nucl. Med. 51 (2021) 157–169, https://doi.org/10.1053/j.semnuclmed.2020.10.003.

[15] C. Cohade, M. Osman, L.T. Marshall, R.L. Wahl, PET-CT: accuracy of PET and CT spatial registration of lung lesions, Eur. J. Nucl. Med. Mol. Imag. 30 (2003) 721–726, https://doi.org/10.1007/s00259-002-1055-3.

[16] M.M. Osman, C. Cohade, Y. Nakamoto, L.T. Marshall, J.P. Leal, R.L. Wahl, Clinically significant inaccurate localization of lesions with PET/CT: frequency in 300 patients, J. Nucl. Med. 44 (2003).

[17] A. Dimitrakopoulou-Strauss, L. Pan, L.G. Strauss, Quantitative approaches of dynamic FDG-PET and PET/CT studies (dPET/CT) for the evaluation of oncological patients, Cancer Imag. 12 (2012) 283–289, https://doi.org/10.1102/1470-7330.2012.0033.

[18] M. Muzi, F. O'Sullivan, D.A. Mankoff, R.K. Doot, L.A. Pierce, B.F. Kurland, H. M. Linden, P.E. Kinahan, Quantitative assessment of dynamic PET imaging data in cancer imaging, Magn. Reson. Imag. 30 (2012) 1203–1215, https://doi.org/10.1016/j.mri.2012.05.008.

[19] M. Westerterp, J. Pruim, W. Oyen, O. Hoekstra, A. Paans, E. Visser, J. van Lanschot, G. Sloof, R. Boellaard, Quantification of FDG PET studies using standardised uptake values in multi-centre trials: effects of image reconstruction, resolution and ROI definition parameters, Eur. J. Nucl. Med. Mol. Imag. 34 (2007) 392–404, https://doi.org/10.1007/s00259-006-0224-1.

[20] M.L. Calcagni, M.V. Mattoli, M.A. Blasi, G. Petrone, M.G. Sammarco, L. Indovina, A. Mulè, V. Rufini, A. Giordano, A prospective analysis of ^{18}F-FDG PET/CT in patients with uveal melanoma: comparison between metabolic rate of glucose (MRglu) and standardized uptake value (SUV) and correlations with histopathological features, Eur. J. Nucl. Med. Mol. Imag. 40 (2013) 1682–1691, https://doi.org/10.1007/S00259-013-2488-6.

[21] E. Laffon, M.L. Calcagni, G. Galli, A. Giordano, A. Capotosti, R. Marthan, L. Indovina, Comparison of three-parameter kinetic model analysis to standard Patlak's analysis in 18 F-FDG PET imaging of lung cancer patients, EJNMMI Res. 8 (2018), https://doi.org/10.1186/S13550-018-0369-5.

[22] M.L. Calcagni, L. Indovina, D. di Franco, V. Rufini, L. Leccisotti, A. Giordano, G. Galli, Are the simplified methods to estimate K i in 18 F-FDG PET studies feasible in clinical routine? Comparison between three simplified methods, Q. J. Nucl. Med. Mol. Imag. 62 (2018) 190–199, https://doi.org/10.23736/S1824-4785.16.02742-4.

[23] N.C. Krak, R. Boellaard, O.S. Hoekstra, J.W.R. Twisk, C.J. Hoekstra, A. A. Lammertsma, Effects of ROI definition and reconstruction method on quantitative outcome and applicability in a response monitoring trial, Eur. J. Nucl. Med. Mol. Imag. 32 (2005) 294–301, https://doi.org/10.1007/s00259-004-1566-1.

[24] R. Boellaard, N.C. Krak, O.S. Hoekstra, A. a Lammertsma, C.J. Jaskowiak, J. a Bianco, S.B. Perlman, J.P. Fine, 圭一松本 英彦表, Effects of noise, image resolution, and roi definition on the accuracy of standard uptake values: a simulation study, J. Nucl. Med. : Off. Publ. Soc. Nuclear Med. 45 (2002) 670–678. http://www.ncbi.nlm.nih.gov/pubmed/15750154%5Cnhttp://www.ncbi.nlm.nih.gov/pubmed/15347719.

[25] R.K. Doot, J.S. Scheuermann, P.E. Christian, J.S. Karp, P.E. Kinahan, Instrumentation factors affecting variance and bias of quantifying tracer uptake with PET/CT, Med. Phys. 37 (2010) 6035–6046, https://doi.org/10.1118/1.3499298.

[26] S. Mansor, E. Pfaehler, D. Heijtel, M.A. Lodge, R. Boellaard, M. Yaqub, Impact of PET/CT system, reconstruction protocol, data analysis method, and repositioning on PET/CT precision: an experimental evaluation using an oncology and brain phantom: an, Med. Phys. 44 (2017) 6413–6424, https://doi.org/10.1002/mp.12623.

[27] J.T. Kuikka, J.B. Bassingthwaighte, M.M. Henrich, L.E. Feinendegen, Mathematical modelling in nuclear medicine, Eur. J. Nucl. Med. 18 (1991) 351–362, https://doi.org/10.1007/BF02285464.

[28] H. Watabe, Y. Ikoma, Y. Kimura, M. Naganawa, M. Shidahara, PET kinetic analysis - compartmental model, Ann. Nucl. Med. 20 (2006) 583–588, https://doi.org/10.1007/BF02984655.

[29] M. Bentourkia, H. Zaidi, Tracer kinetic modeling in PET, Pet. Clin. 2 (2007) 267–277, https://doi.org/10.1016/j.cpet.2007.08.003.

[30] L. Pan, C. Cheng, U. Haberkorn, A. Dimitrakopoulou-Strauss, Machine learning-based kinetic modeling: a robust and reproducible solution for quantitative analysis of dynamic PET data, Phys. Med. Biol. 62 (2017) 3566–3581, https://doi.org/10.1088/1361-6560/aa6244.

[31] T. WD, B. E, N. M, N. AG, G. KR, Y. Y, B. DG, P. CA, R. GJ, V.S. PE, G. K, A. JH, A. H, R. VW, H. FR, S. G, M. T, H. RM, I. Y, J. J, S.-C. M, S. JP, T. T, T. M, V. J, W. I, Y. PC, A. D, B. C, F. D, F. W, G. A, G. M, H. P, H. D, J. B, J. D, K. K, K. K, L. JS, M. VA, P. I, R. V, R. R, S. N, T. E, T. M, Y. D, International association for the study of lung cancer/american thoracic society/european respiratory society international multidisciplinary classification of lung adenocarcinoma, J. Thorac. Oncol. : Off. Publ. Int. Associat. Study of Lung Cancer 6 (2011) 244–285, https://doi.org/10.1097/JTO.0B013E318206A221.

[32] J.A. Barta, C.A. Powell, J.P. Wisnivesky, Global epidemiology of lung cancer, Ann. Glob. Health 85 (2019), https://doi.org/10.5334/AOGH.2419.

[33] E. Silvestri, V. Scolozzi, G. Rizzo, L. Indovina, M. Castellaro, M.V. Mattoli, P. Graziano, G. Cardillo, A. Bertoldo, M.L. Calcagni, The kinetics of 18F-FDG in lung cancer: compartmental models and voxel analysis, EJNMMI Res. 8 (2018) 1–8, https://doi.org/10.1186/S13550-018-0439-8, 2018, 1–10.

[34] S. Berg, D. Kutra, T. Kroeger, C.N. Straehle, B.X. Kausler, C. Haubold, M. Schiegg, J. Ales, T. Beier, M. Rudy, K. Eren, J.I. Cervantes, B. Xu, F. Beuttenmueller, A. Wolny, C. Zhang, U. Koethe, F.A. Hamprecht, A. Kreshuk, ilastik: interactive machine learning for (bio)image analysis, Nat. Methods 16 (2019) 1226–1232, https://doi.org/10.1038/s41592-019-0582-9.

[35] M. Pal, Random forest classifier for remote sensing classification, Int. J. Rem. Sens. 26 (2005) 217–222, https://doi.org/10.1080/01431160412331269698.

[36] C. Sommer, U. Köthe, C. Straehle, F.A. Hamprecht, Ilastik: Interactive Learning and Segmentation Toolkit Learning Complex Stochastic Models with Invertible Neural Networks: a New Approach to Bayesian Inference View Project Ilastik: Interactive Learning and Segmentation Toolkit, 2011, https://doi.org/10.1109/ISBI.2011.5872394.

[37] A. Kreshuk, C. Zhang, Machine learning: advanced image segmentation using ilastik, in: Methods in Molecular Biology, Humana Press Inc., 2019, pp. 449–463, https://doi.org/10.1007/978-1-4939-9686-5_21.

[38] S. Takahama, Y. Kurose, Y. Mukuta, H. Abe, M. Fukayama, A. Yoshizawa, M. Kitagawa, T. Harada, Multi-Stage Pathological Image Classification Using Semantic Segmentation, 2019.

[39] H. Yu, Z. Yang, L. Tan, Y. Wang, W. Sun, M. Sun, Y. Tang, Methods and datasets on semantic segmentation: a review, Neurocomputing 304 (2018) 82–103, https://doi.org/10.1016/j.neucom.2018.03.037.

[40] A. Almuhaideb, N. Papathanasiou, J. Bomanji, 18F-FDG PET/CT imaging in oncology, Ann. Saudi Med. 31 (2011) 3–13, https://doi.org/10.4103/0256-4947.75771.

[41] C. Cohade, M. Osman, L.T. Marshall, R.L. Wahl, PET-CT: accuracy of PET and CT spatial registration of lung lesions, Eur. J. Nucl. Med. Mol. Imag. 30 (2003) 721–726, https://doi.org/10.1007/s00259-002-1055-3.

[42] M.M. Osman, C. Cohade, Y. Nakamoto, L.T. Marshall, J.P. Leal, R.L. Wahl, Clinically significant inaccurate localization of lesions with PET/CT: frequency in 300 patients, J. Nucl. Med. 44 (2003).

[43] Z. Yang, K. Li, Y. Guo, H. Ma, M. Zheng, Compact real-valued teaching-learning based optimization with the applications to neural network training, Knowl. Base Syst. 159 (2018) 51–62, https://doi.org/10.1016/J.KNOSYS.2018.06.004.

[44] G. Bianchetti, F. Ciccarone, M.R. Ciriolo, M. de Spirito, G. Pani, G. Maulucci, Label-free metabolic clustering through unsupervised pixel classification of multiparametric fluorescent images, Anal. Chim. Acta 1148 (2021) 238173, https://doi.org/10.1016/j.aca.2020.12.048.

[45] G. Bianchetti, M. de Spirito, G. Maulucci, Unsupervised clustering of multiparametric fluorescent images extends the spectrum of detectable cell membrane phases with sub-micrometric resolution, Biomed. Opt Express 11 (2020) 5728, https://doi.org/10.1364/BOE.399655.

[46] G. Bianchetti, F. di Giacinto, M. de Spirito, G. Maulucci, Machine-learning assisted confocal imaging of intracellular sites of triglycerides and cholesteryl esters formation and storage, Anal. Chim. Acta 1121 (2020) 57–66, https://doi.org/10.1016/j.aca.2020.04.076.

[47] Z. Wu, H. Zhu, G. Li, Z. Cui, H. Huang, J. Li, E. Chen, G. Xu, An efficient Wikipedia semantic matching approach to text document classification, Inf. Sci. 393 (2017) 15–28, https://doi.org/10.1016/J.INS.2017.02.009.

[48] Z. Wu, L. Lei, G. Li, H. Huang, C. Zheng, E. Chen, G. Xu, A topic modeling based approach to novel document automatic summarization, Expert Syst. Appl. 84 (2017) 12–23, https://doi.org/10.1016/J.ESWA.2017.04.054.

[49] Z. Wu, S. Shen, X. Lian, X. Su, E. Chen, A dummy-based user privacy protection approach for text information retrieval, Knowl. Base Syst. 195 (2020), 105679, https://doi.org/10.1016/J.KNOSYS.2020.105679.

[50] W. Yan, G. Li, Z. Wu, S. Wang, P.S. Yu, Extracting diverse-shapelets for early classification on time series, World Wide Web 23 (2020) 3055–3081, https://doi.org/10.1007/S11280-020-00820-Z/FIGURES/16.